Check for updates

Structural and electronic properties of MXene flakes: from edge effects to bandgap evolution

Miquel Allés, [ID] [a] Sergi Vela, [ID] [b] Ángel Morales-García, [ID] [a] Francesc Viñes [ID] [a] and Carmen Sousa [ID] *[a]

The structural and electronic properties of MXenes were investigated by means of a finite-system approach using all-electron Density Functional Theory-based calculations. Pristine $(M_2C)_n$ flakes and their O-terminated counterparts $(M_2CO_2)_n$ (M = Sc, Y, Ti, Zr, Hf, V, Nb, Ta, Cr, Mo and W; $12 \leq n \leq 216$) were computationally modelled. Surface-like behaviour is lost for $n \leq 90$, corresponding to ca. 3 nm wide flakes, where finite-size effects become increasingly relevant. While the flake structure at the core is very similar to that found in extended periodic models, the edges are often deformed due to structural defects, which impact their electronic properties. Pristine M_2C flakes are metallic, while the O-terminated M_2CO_2 counterparts present bandgaps exceeding 1 eV for metals of Groups III and IV when neglecting low-populated gap states near the Fermi level. The alignment of the valence and conduction bands for these systems evolves favourably to nearly include the water splitting half-reactions within the bandgap for the largest flakes. Overall, our results show that Sc, Y, Zr, and Hf O-functionalised MXenes are the best suited for photocatalytic water splitting, obtaining energy gaps within the visible spectrum for several flake sizes, and band alignments closer to water oxidation and hydrogen reduction reactions.

1. Introduction

Two-dimensional (2D) materials have gained popularity since the discovery of graphene in 2004 by Novoselov and colleagues.[1] Graphene is considered as the archetype material in the field due to its remarkable mechanical, electrical, and thermal properties.[2] More importantly, its isolation established new exfoliation procedures opening the door to a broad family of 2D materials. Early research was primarily focused on graphene itself and structurally-similar compounds like hexagonal boron nitride (*h*-BN).[3] Other families of compounds were soon discovered, incorporating transition metals (Transition Metal Dichalcogenides[4] and MXenes[5]) or organic components (*e.g.* Covalent–Organic Frameworks[6–8]) into their chemical formulae. This growing diversity led to the discovery of systems with exceptional properties and applications ranging from energy storage to photocatalysis.[9–11]

Among them, MXenes, a family of 2D materials first discovered in 2011 by Naguib and coworkers,[12] are typically synthesised following a top-down procedure from their three-dimensional precursors known as MAX phases, with the

aDepartament de Ciència de Materials i Química Física & Institut de Química Teòrica i Computacional (IQTCUB), Universitat de Barcelona, c/Martí i Franquès 1-11, 08028 Barcelona, Spain. E-mail: c.sousa@ub.edu
bInstitut de Química Avançada de Catalunya (IQAC-CSIC), c/Jordi Girona 18-26, 08028 Barcelona, Spain

$M_{n+1}AX_n$ chemical formula. There, M represents an early transition metal from groups III to VI, A is a p-block element, and X is either carbon or nitrogen. The *n* number, ranging from 1 to 4, defines the thickness of the resulting MXene layers.[13–16] The final MXene material is defined by the $M_{n+1}X_nT_x$ chemical formula, where T_x are terminations that arise from the synthetic procedure or the working conditions. Typically, hydrofluoric acid (HF) is used as the selective chemical etching agent of the A layer, resulting in MXenes with –F, –H, –O, and –OH terminal groups.[17,18] Still, the selective etching of A using molten salts can lead to other terminations, such as –S, –Se, –Te, –NH, –Cl, –Br.[19] In some cases, it is even possible to obtain pristine MXenes, without surface terminations, with $M_{n+1}X_n$ stoichiometry.[19] Here, we focus our study on the most common –O termination.

From a structural perspective, pristine MXenes can adopt two different hexagonal stackings, ABA or ABC, which depend on the mutual alignment of M and X layers, while always maintaining the M–X–M sequence (see Fig. 1). The ABC stacking was found to be mainly stable for Sc, Y, Ti, Zr, Hf, V, Nb, and Ta-based MXenes, while the ABA stacking was mostly preferred for Mo and W-based MXenes.[20] Additionally, for Cr-based MXenes, both structures were found to be quite competitive, ABC stacking still being slightly favoured (0.02 eV per Cr_2C unit) in its pristine form, while ABA is preferred when functionalised with O atoms (0.59 eV per Cr_2CO_2 unit).[20] Upon functionalisation, different configurations may arise from each
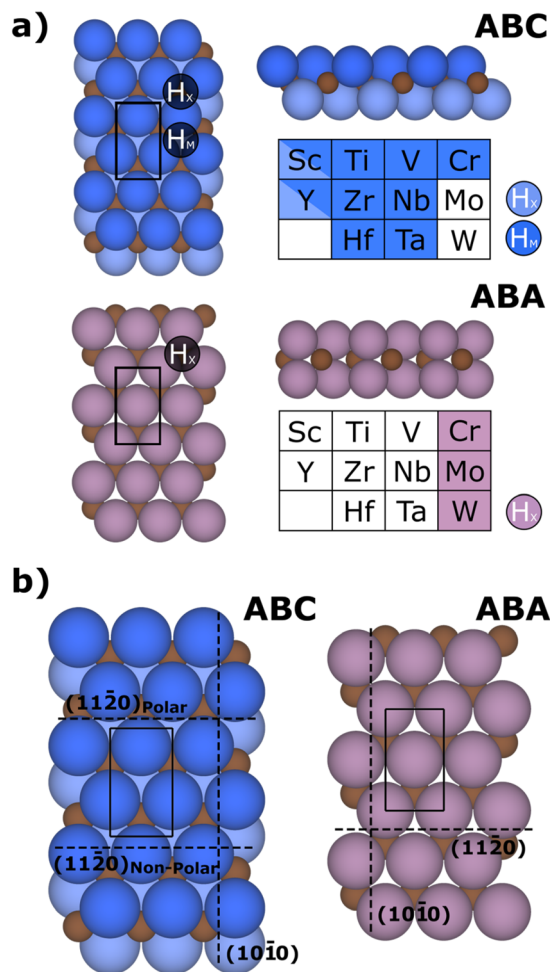
Fig. 1 (a) Top (left) and side (right) views of pristine MXenes for ABC (top) and ABA (bottom) stackings. (b) Representation of the $(10\bar{1}0)$ and $(11\bar{2}0)$ surfaces on ABC and ABA stacking. Metallic atoms are shown as blue or purple spheres, while carbons are represented as brown spheres. For ABC, the top layer is represented in darker blue to differentiate from bottom (lighter colour) layer. Black lines represent $c(1 \times 1)$ cells.

stacking, depending on which surface sites the T_x termination occupies. For ABC stacking, T_x can occupy either the H_M hollow site located on top of the outermost metallic layer, or the H_X hollow site positioned above the carbon layer, including mixed configurations for Sc and Y, H_{MX}, consisting of H_M adsorption sites on one face and H_X on the other—effectively Janus type of structures. Alternatively, for ABA stacking cases, only H_X sites have been defined, with terminations located on top of the central C layer. These former studies have been taken into account here, and we only consider the most stable stacking and adsorption sites of the experimentally synthesised MXenes.[20,21]

From an electronic structure perspective, the magnetic configuration of some pristine MXenes (these are Ti_2C, Zr_2C, Hf_2C, and Cr_2C) has been reported to be antiferromagnetic, with antiparallel spins located on the metallic atoms in the top and bottom layers (one layer being entirely spin-up and the

other entirely spin-down).[22] In contrast, no stable magnetic configurations have been reported for other pristine MXenes, nor any functionalised MXenes, regardless of the surface termination.[20] For now, all studied pristine MXenes have been reported to be metallic, so the creation of a bandgap depends on the surface functionalisation or the material nanoengineering. Concerning the former, O-terminated MXenes show an intrinsic semiconducting behaviour for most Group III, IV, and VI transition metal-based structures, with bandgaps lying within the visible spectrum, which could make them suitable candidates for photocatalytic applications.[20] As far as the nanoengineering aspect is concerned, the size control of pristine MXene flakes can open the bandgap and modulate its size.[23]

From a computational point of view, the majority of studies on MXenes use periodic atomic models (i.e., slab models) to rationalize and predict their experimental structure and properties.[11,15,20,22] In some cases, these studies have been extended to modelling one-dimensional nanoribbons, aiming to capture edge effects and finite-size phenomena.[24–26] While these slab models successfully reproduce several structural and electronic properties of MXenes, realistic MXene models need to mimic finite flakes, whose morphology and electronic properties strongly rely on synthesis-dependent factors such as termination chemistry, defects, oxidation state, and flake morphology.[27,28] Depending on the preparation route, various Ti-containing MXene flakes of different sizes have been obtained, with thicknesses ranging between 1–5 nm and lateral sizes ranging from a few μm to less than 500 nm.[27,29] Recently, MXene 0D quantum dots (QD), with lateral sizes smaller than 10 nm, have also been synthesised.[30,31] These experimental studies demonstrated that the average size, shape, and properties of MXene QD can be tailored by selecting the appropriate reaction conditions, paving the way for tunable properties. Despite their relevance, computational studies explicitly using finite models of MXene flakes remain to date scarce. Only Ti_2C and Ti_2CO_2 flakes as finite systems of varying sizes have been investigated,[23,32] confirming the antiferromagnetic behaviour of the non-terminated Ti_2C flakes,[23] and revealing significant differences in energy gap values for O-functionalised systems when compared to periodic models, which calls for a broader study on how to model MXenes in a more representative manner.

In this work, we present a systematic high-throughput computational study to investigate the structural and electronic properties of a total of 176 pristine (M_2C) and O-terminated (M_2CO_2) MXene flakes, covering eleven transition metals of Groups III–VI (M = Sc, Y, Ti, Zr, Hf, V, Nb, Ta, Cr, Mo, and W) and different flake sizes with diameters ranging from 0.7 to almost 6 nm. This study encompasses the formation of flakes following a top-down scheme based on Wulff construction principles,[33] which identify the most stable shapes by minimising the surface energy. The fully optimised structures were obtained using Density Functional Theory (DFT), showing convergence towards slab models as flakes grow. In addition, the bandgap evolution was analysed for all O-functionalized

MXene flakes, by means of hybrid exchange–correlation functional calculations. The most promising candidates to overcome photocatalytic reactions were further analysed, and their bandgap alignment with respect to the water splitting reaction was determined. Finally, this study identifies the best suited O-functionalized MXene flakes capable of driving photocatalytic water splitting under the solar spectrum.

2. Models and methods

2.1 Construction of the $(M_2C)_n$ and $(M_2CO_2)_n$ flakes

Initially, the most stable conformations of pristine 2D MXenes were acquired (see Fig. 1) following the most stable stackings as previously reported for periodic models.[20] Periodic calculations of orthorhombic $c(1 \times 1)$ M_2C unit cells were thus performed for all conformations, followed by structure optimisations. To construct the MXene flakes (0D) based on Wulff's approach, cleavage energies of the relevant crystallographic planes need to be computed. Starting from a 2D material, the resulting surface cuts reduce the system dimensionality, producing one-dimensional nanoribbons. Hence, to compute the cleavage energy, the $c(1 \times 1)$ cell was enlarged to a $c(3 \times 3)$ supercell to ensure sufficient separation between the two surfaces created when defining nanoribbons (see Fig. S1 of the SI). This choice prevents structural and electronic interactions between opposite surfaces within the same nanoribbon, that may arise if the nanoribbon is too narrow. MXenes present (0001) surfaces on basal planes, while (10$\bar{1}$0) and (11$\bar{2}$0) surfaces are the most stable low Miller indices cuts for both ABA and ABC stacking conformations (see Fig. 1). On ABA stacking structures, there is only one possible cut regardless the surface, while for ABC stacking, two different cuts for the (11$\bar{2}$0) surface are possible; i.e. (11$\bar{2}$0)$_{polar}$ and (11$\bar{2}$0)$_{non-polar}$. Polar (11$\bar{2}$0) surface exposes two faces, one displaying C atoms, while the other face shows metallic atoms. The non-polar (11$\bar{2}$0) surface exposes two symmetrical faces having both metal and C atoms. This led to two different, but stoichiometrically equivalent, $c(3 \times 3)$ unit cells for ABC stacking. Starting from $c(3 \times 3)$ supercells, MXene nanoribbons were defined by introducing a 10 Å vacuum region along the direction normal to the (10$\bar{1}$0) and (11$\bar{2}$0) surfaces and subsequently reoptimized, in order to obtain the cleavage energy ($E_{Cleavage}$) of each face relative to the periodic structure, defined as

$$E_{Cleavage} = \frac{E_{Nanoribbon} - E_{Surf}}{A} \qquad (1)$$

where $E_{Nanoribbon}$ is the energy of the $c(3 \times 3)$ supercell with the additional vacuum spacing, containing the nanoribbon, E_{Surf} is the energy of the $c(3 \times 3)$ supercell that represents the 2D surface, and A is the area of the exposed surface generated due to the vacuum addition when creating the nanoribbon.

To model the MXene flakes using the gained $E_{Cleavage}$, the Wulffpack python package,[34] developed following Wulff's construction theorem to minimise the surface/cleavage energy when creating geometric structures, was used. This software generates flakes by replicating and cutting the periodic $c(1 \times 1)$ structure, taking into account the computed cleavage energy for each crystallographic plane and the approximate number of atoms of the desired flake. This procedure led us with highly symmetric, yet not stoichiometric, MXene flakes. To obtain stoichiometric structures, terminal atoms had to be removed one by one on different sites, reoptimising the isomers, and selecting the most stable ones. Finally, the stoichiometric structures, $(M_2C)_n$, with n ranging from 12 to 216, were fully optimised by DFT calculations.

To properly functionalise the flakes, we made use of the optimised geometries obtained during the relaxation of pristine flakes. A stoichiometric number of oxygen atoms was placed on each surface at the previously identified most stable adsorption sites (see Fig. 1), with an initial O-surface distance set to 1.2 Å. All $(M_2CO_2)_n$ systems were then fully reoptimised, allowing the oxygen atoms, particularly those at the edge regions, to rearrange in their most-stable O-functionalised configurations.

The energy difference between flakes and periodic surfaces was evaluated by comparing the flake energy per stoichiometric unit referred to the slab model, defined as

$$\Delta E = \frac{E_{Flake}}{n} - E_{Slab} \qquad (2)$$

where E_{Flake} is the energy of the optimised finite flake, n corresponds to the number of stoichiometric units of the flake, and E_{Slab} is half of the energy of each M_2C/M_2CO_2 $c(1 \times 1)$ unit cell, yielding the energy of one stoichiometric unit of M_2C/M_2CO_2 in the periodic 2D system. Notice that normalisation of E_{Surf} by the eighteen stoichiometric units contained in the $c(3 \times 3)$ surface cell, leads to the same value as E_{Slab}.

2.2 Computational details

All DFT calculations were carried out using the Fritz-Haber Institute Ab Initio Materials Simulation (FHI-AIMS) software,[35] which uses Numeric Atom-centered Orbitals (NAO) as a basis set and explicitly considers all electrons. For the exchange and correlation approximation, the PBE functional[40] was chosen, taking into account relativistic effects through the Zeroth Order Regular Approximation (ZORA),[35] with a light Tier-1 NAO basis set.[36] All atomic forces were converged below 10^{-2} eV Å^{-1}, using the Broyden-Fletcher-Goldfarb-Shanno (BFGS) optimisation algorithm, while the criterion for the self-consistent field was defined at 10^{-5} eV, setting a Gaussian broadening of 0.01 eV. For periodic calculations, a grid of $7 \times 7 \times 1$ k-points was used with a more restrictive force convergence threshold of 10^{-3} eV Å^{-1}.

Spin-polarised effects were assessed through single-point calculations on Ti-, Zr-, Hf- and Cr-based flakes, as these are the compounds for which antiferromagnetic behaviour was found in the periodic systems. For Ti$_2$C MXene, the energy difference between spin-polarised and non-spin polarised states is 0.12 eV in favour of the antiferromagnetic configuration under periodic boundary conditions.[22] In the case of Ti$_2$C finite flakes, the energy difference per stoichiometric unit

increases with the size of the flake, preferring the antiferromagnetic configuration but staying below 0.1 eV. In contrast, Zr, Hf and Cr-based pristine MXene flakes mostly converged on non-magnetic configurations, with some exceptions in which the antiferromagnetic state appears *ca.* 0.01 eV (per stoichiometric unit) lower in energy. The overall energy differences between magnetic and non-magnetic configurations remain small enough to justify the use of non-spin polarised calculations for the remainder of the study, as they provide a reasonable approximation while significantly reducing computational cost. Furthermore, no magnetic behaviour has been reported for O-terminated systems, either in periodic structures or in finite flakes. To properly estimate the bandgap values, additional single-point calculations using the hybrid PBE0 exchange–correlation functional[37] were carried out on geometries previously optimised at PBE level. In general, PBE0 yields bandgaps that are closer to reference GW estimates;[15] however, structural variations in finite systems may modify this correlation.

3. Results and discussion

3.1 Structural analysis

A total of 176 MXene flakes were modelled, including both pristine $(M_2C)_n$ and O-terminated $(M_2CO_2)_n$ structures. The flakes were built following Wulff's construction rules based on cleavage energy calculations (see Table S1 of the SI), as described in the Models and methods section, with diameters between 0.7 and 5.7 nm. For MXenes with ABC stacking, seven flake sizes were generated—n = 18, 36, 60, 90, 126, 168, and 216—due to the dominance of the $(11\bar{2}0)$ non-polar surface in all cases. These flakes showed a hexagonal shape, as can be seen in Fig. 2.

For MXenes displaying ABA stacking, the similar cleavage energies between the $(10\bar{1}0)$ and $(11\bar{2}0)$ facets resulted in specific flake morphologies and sizes. In particular, eight flake

sizes were obtained for Cr—n = 12, 30, 57, 90, 111, 156, 183, and 210—, nine for Mo—n = 12, 30, 54, 72, 84, 108, 150, 180, and 198 units—, and eight for W—n = 12, 30, 42, 67, 105, 147, 177, and 195. For the O-terminated flakes, only the most stable oxygen adsorption sites were considered, shown in Fig. 1. Metal hollow (H_M) and carbon hollow (H_X) sites were selected for ABC and ABA structures, respectively, except for Sc and Y, for which the H_{MX} structure (a mixture of H_M and H_X sites on opposite MXene surfaces) was earlier found to be more stable.[15]

The representation of the energy difference per stoichiometric unit between flakes and $c(1 \times 1)$ periodic surface (eqn (2)) against n allows one to set the threshold size that shows asymptotic behaviour to the periodic surface. This energy difference is expected to be dominated by edge contributions and to decay towards zero when increasing flake size. As can be seen in Fig. S2 of the SI, flakes with $n \geq 90$ are large enough to reproduce surface-like properties at their core, whereas smaller flakes behave as finite systems. However, ΔE could only be considered size-independent for flakes containing more than 168 stoichiometric units. Alternatively, the energy difference per stoichiometric unit between flakes and $c(1 \times 1)$ periodic surface, ΔE, can be plotted against the number of units to the power of $-1/2$ (see Fig. 3). This factor follows the spherical cluster approximation[38] to evaluate the convergence of flakes to periodic structure, modifying the $n^{-1/3}$ representation for 3D systems to $n^{-1/2}$ for 2D materials, as it has been shown to work previously on 2D and 3D systems.[39] Focusing on pristine structures, all cases exhibit excellent linear fits, with regression coefficient, R, values above 0.995, except for Cr with ABA stacking, which is not the most stable conformation for pristine Cr-MXene (see Table S2 of the SI). Interceptions are below 0.053 eV in absolute value, with slopes increasing along periods across Groups IV, V and VI.

In the case of O-functionalised systems (see Fig. S3 and Table S2 of the SI), larger deviations are observed, with a maximum intercept of 0.289 eV for Ti. Despite this, strong
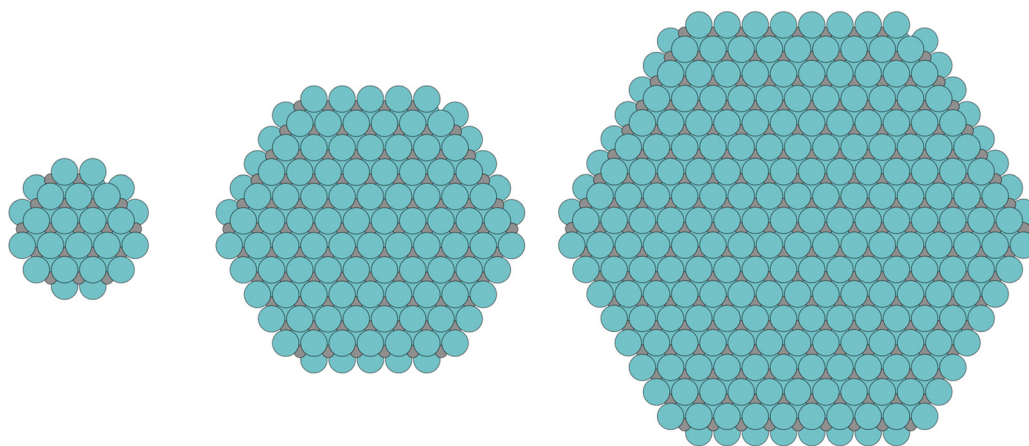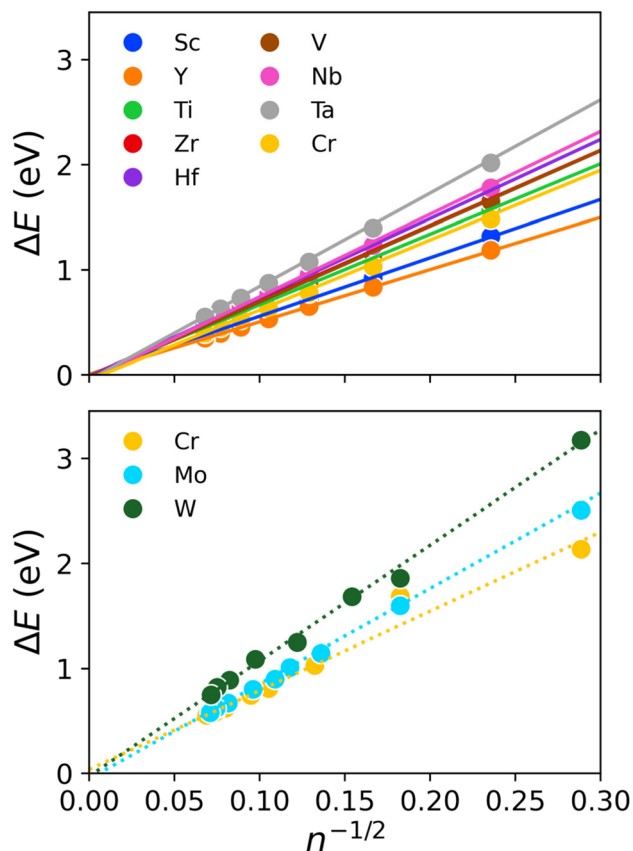

Fig. 2 Top view of $(Nb_2C)_{18}$ (left), $(Nb_2C)_{90}$ (middle), and $(Nb_2C)_{216}$ (right) MXene flakes. Nb and C atoms are shown as turquoise and grey spheres, respectively.

Fig. 3 Differences in energy per stoichiometric unit between flakes and periodic slabs of M_2C MXenes *vs.* number of stoichiometric units (n) of flakes to the power of $-1/2$. The top graph shows ABC stacking with solid lines, while the bottom graph presents ABA stacking using dotted lines. Metals are differentiated by colors, and each MXene is referred to its own slab surface.

linear correlations are maintained, with R values above 0.978 in all cases except for Cr in the ABC stacking, which is not the most stable configuration for O-functionalised Cr-MXene.

An exhaustive structural analysis was carried out as well for all studied systems, extracting the most representative structural parameters. Specifically, average values of the C–C distance, $d(CC)$, the distance between metals on the top layer, $d(M_{top}–M_{top})$, and on the bottom layer, $d(M_{bot}–M_{bot})$, were measured, as they correlate with the lattice parameter a, obtained from periodic calculations, and can be easily compared to experimental data from X-ray diffraction. In addition, average flake thicknesses were estimated, defined as the distance between top and bottom metal layers in M_2C systems, and between oxygen layers in M_2CO_2 structures. The evolution of the parameters for all M_2C and M_2CO_2 flakes is presented in Fig. S4 of the SI, while detailed values for the largest flakes are provided in Table S3 of the SI. For the structural analysis, the largest flake was selected in each case, as structural convergence is observed with increasing flake size, with values approaching those of the corresponding periodic systems.

For M_2C flakes, the results show an excellent agreement with periodic structures as the flake size increases, with only minor variations observed during the growth process. Differences between $d(M_{top}M_{top})$ and $d(M_{bot}M_{bot})$ are generally negligible, while small deviations are seen on $d(CC)$. A comparison between ABA and ABC stackings reveals more compact $d(CC)$ distances in ABA structures, typically compensated by a slight increase in overall flake thickness. Notably, structural parameters obtained from periodic calculations fall within the range defined by the $d(CC)$, $d(M_{top}M_{top})$, and $d(M_{bot}M_{bot})$ distances measured in the flakes.

In the case of M_2CO_2 flakes, the introduction of O terminations leads to some structural changes. The specific adsorption site of the O atoms significantly affects the average interlayer metal distances, especially in cases where different adsorption geometries are adopted on the top and bottom surfaces, *e.g.*, Sc and Y, causing sizeable distortions in $d(M_{top}M_{top})$, $d(M_{bot}M_{bot})$, and $d(CC)$ parameters. Despite these localised distortions, most systems display average bond distances and geometrical parameters that remain close to those obtained from periodic structures.

The thickness of M_2C flakes shows a general increasing trend along periods and groups, consistent with the atomic radii of the constituent elements, but differentiating between ABC and ABA structures, with some deviations on ABA cases. A good agreement is observed when comparing thickness with periodic data. For the case of functionalised flakes, thickness depends on termination sites, obtaining higher values for H_X sites, followed by H_M, and H_{MX}, respectively. When comparing with periodic models, noticeable thickness changes are seen for ABA-stacked structures and systems with asymmetric O adsorption. In contrast, ABC flakes with H_M adsorption sites match more closely with values predicted by periodic models.

To further evaluate structural convergence with size, besides the average distances, the internal bond distances across each flake were also analysed. As illustrated as a heat map in Fig. 4 for the Ti_2CO_2 system and the $d(CC)$, central atoms exhibit distances nearly identical to the corresponding periodic lattice parameter, while edge atoms show small deviations due to undercoordination. These deviations are seen for all MXenes flakes, but are more pronounced in smaller flakes, where edge effects dominate, becoming less significant as the flake size increases. Importantly, deviations are not always skewed in one direction; in many cases, opposing distortions cancel out, yielding mean values close to the periodic ones. Similar trends are observed for the $d(M_{top}M_{top})$, $d(M_{bot}M_{bot})$, and the thickness of the flakes.

Beyond the specific structural analyses, a general inspection of the flakes reveals slight in-plane deformations in pristine ABC-stacked Ti, V, and Cr-based flakes containing 90 or more stoichiometric units. These flakes typically exhibit two distinct types of out-of-plane distortion: a "three-up/three-down" edge bending, as observed in all V and Cr flakes with $n \geq 90$, and in the $(Ti_2C)_{168}$ flake, or a global curvature affecting the entire flake, seen in all other Ti flakes. Upon O-functionalisation, these distortions become more generalised, particularly in
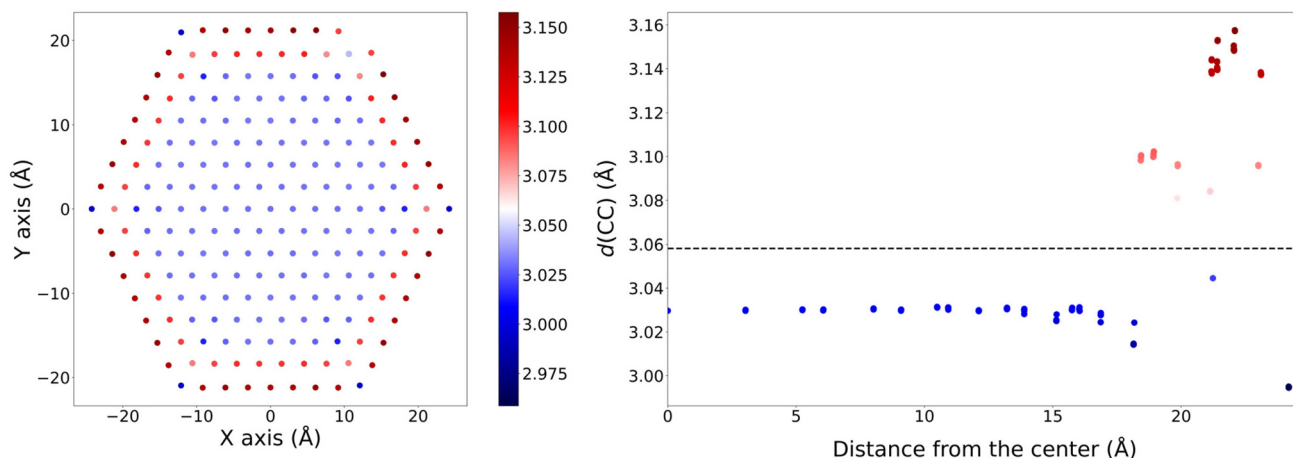
Fig. 4 Spatial distribution (left) and radial evolution (right) of d(CC) in $(Ti_2CO_2)_{216}$ flake (values in Å). The colour scale on the left plot bond average length deviations while in the right plot, each point represents average bond lengths as a function of its distance from the centre, with the dashed line indicating the mean d(CC) value of the flake.

ABC-stacked flakes. In these cases, the three-up/three-down edge bending is consistently observed for all H_M-functionalised structures irrespective of the metal and particle size, while the H_{MX} O-terminated Sc and Y flakes display a characteristic U-shaped curvature, with H_M-adsorbed oxygen atoms located on the inner side and oxygen atoms adsorbed on a H_X site on the outer surface. In contrast, ABA-stacked flakes remain largely planar, exhibiting no significant deformation aside from the lateral vacancies introduced to preserve stoichiometry. An illustrative example of these deformations can be found in Fig. 5 for $(Sc_2CO_2)_{216}$ and $(Ti_2CO_2)_{216}$ flakes.

3.2 Electronic analysis

The optical properties of pristine and O-functionalised flakes are studied using the bandgap energies, E_g, as well as the HOMO–LUMO gaps, E_{HL}. E_g is extracted from the Density Of States (DOS), and is a common metric to analyse periodic systems, while E_{HL} is common when analysing finite systems. Being at the crossover, where we combine both perspectives.

For pristine MXenes, calculations using Perdew–Burke–Ernzerhof (PBE)[40] exchange–correlation functional do not

Fig. 5 $(Sc_2CO_2)_{216}$ (top) and $(Ti_2CO_2)_{216}$ (bottom) flakes as examples for U-shaped and three-up/three-down edge bending, respectively.

show any significant E_{HL} except for Cr and Mo, where small energy differences, of about 0.10–0.15 eV, are observed. When increasing flake size, E_{HL} tends to zero, mimicking the results of periodic pristine 2D MXenes (see Fig. S5 of the SI). More interesting is the study of the O-functionalised flakes, since the corresponding periodic MXenes already show semiconducting properties.[20] The E_{HL} PBE0 energy gaps decrease with size irrespective of the metal (cf. Fig. 6), while further PBE results can be found in Fig. S6 of the SI. Only a few small flakes present E_{HL} values larger than 1.0 eV; $(Zr_2CO_2)_{18}$, $(Zr_2CO_2)_{36}$, $(Zr_2CO_2)_{60}$, $(Hf_2CO_2)_{36}$, $(Ti_2CO_2)_{18}$, $(Y_2CO_2)_{18}$, $(Mo_2CO_2)_{12}$ and $(W_2CO_2)_{12}$. Based on these results, and as previously found for the energy difference per stoichiometric unit between flakes and periodic surface, we can identify two regimes; an asymptotic regime with final E_{HL} values between 0.1 and 0.6 eV depending on the metal ($n \geq 90$), and a non-asymptotic regime ($n < 90$) where the flakes exhibit finite-size behaviour. Thus, $n = 90$, corresponding to flake diameters of about 3 nm, appears as the threshold beyond which the energy gap converges to a stable value. Interestingly, for all metal MXene flakes, these values are significantly smaller than the bandgap estimations of the corresponding periodic slab models, as previously found for Ti MXene flakes.[23]

To shed light on the origin of this discrepancy, the band structure of all systems has been thoroughly analysed. Fig. 7 reports the PBE0-level DOS for O-terminated Sc MXene flakes of increasing size, as a representative example of the general behaviour. Due to quantum confinement effects, a discretisation of the energy levels is observed for the smaller particles, while broader bands become visible for the largest flakes. Here, E_g is computed as the energy difference between the two narrow bands below and above the Fermi level. It can be observed that an increase of the particle size shifts the Conduction Band Minimum (CBM) to lower energies, and the Valence Band Maximum (VBM) to higher energies, hence decreasing the bandgap. A decrease of E_g with increasing par-
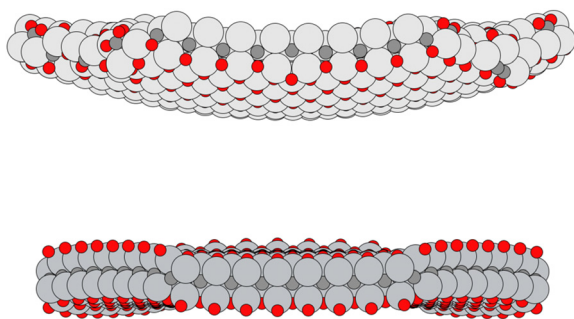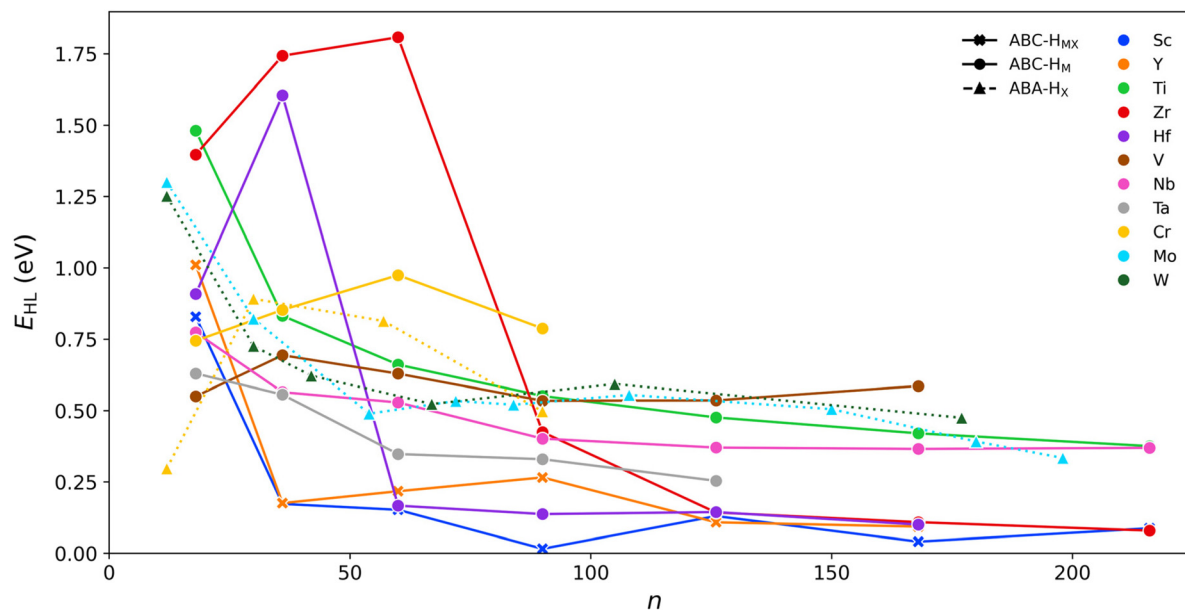
Fig. 6 Evolution of HOMO−LUMO energy gap, E_{HL}, for M_2CO_2 MXenes, as calculated at PBE0 level.

ticle size has also been reported in Ti-MXene nanoparticles.[23,32]

Although small or no bandgaps are observed in large flakes, a region with low occupancy of states appears near E_F in the DOS of the largest Group III, IV, and VI flakes. Further investigation reveals that these gap states are localised on the most external rim for all metals and particle sizes, with the exception of the Ti flakes, where the gap states are associated with defects located on the central carbon atoms. To evaluate the influence of the edge effects on the bandgap, the DOS of the largest flake of each O-terminated MXene was computed when isolating the contribution of atoms located within a radius of 10, 15, 20, and 25 Å of the flake centre. As can be seen in Table 1 and Fig. 8, the gap states gradually disappear (and the bandgap grows) when neglecting the most external atoms, likely due to the aforementioned structural deformations and defects, until they barely contribute to the overall DOS. In fact, this contribution is already small when considering the entire flakes, ranging from 2.75% to 9.26% of the integrated DOS near E_F depending on the metal. This implies that the probability that an excitation will involve those states is very low, preferring the highly populated bands above and below the gap state. Owing to this, from now on we will provide corrected bandgap values (E_g^c), i.e. those ignoring the gap states, to characterise the electronic properties of the MXene flakes.

For Ti-based MXene particles, the gap states originate in defects localised on the central carbon atoms rather than at the edges, so they persist even when the atomic boundary used in the DOS calculations is reduced, leading to a vanishing bandgap. Inspection of the PBE0 DOS for O-terminated Ti MXenes across different flake sizes (see Fig. S7 of the SI) reveals a single, narrow mid-gap band. The prominence of this

band decreases with increasing flake size, as the proportion of central defects diminishes. The contribution of this gap state to the total DOS near E_F is minimal, only 0.34%. Hence, for larger Ti MXene flakes ($n > 90$), the corrected bandgap can be reliably estimated by disregarding these highly localised mid-gap states.

With this in mind, corrected bandgaps of 2.72 (Sc_2CO_2) and 2.29 eV (Y_2CO_2) are obtained for functionalised flakes with O on H_{MX} sites, and Group IV flakes display E_g^c between 0.88 and 1.57 eV. In contrast, Group V and VI flakes remain metallic, in accordance with periodic slab models for Group V, but not for Group VI, that present small bandgaps on periodic models.[20] The reported E_g^c are between 0.23 and 1.86 eV smaller to those obtained from slab periodic models (cf. Table 1), consequently explaining the metallic character of Group VI due to their small estimated bandgap. This E_g^c values lead to corrected Fermi energies (E_F^c), defined here as the valence band maximum (VBM) energies, as the E_F shifts to more negative values when the bandgap widens.

To further evaluate the potential photocatalytic properties of the MXene flakes with semiconductor character, the alignment of the valence and conduction bands edges with respect to the redox potential of the half reactions has to be evaluated. This is shown in Fig. S8 of the SI for the water-splitting process, for which the potentials for water oxidation and hydrogen reduction are −5.67 and −4.44 eV, respectively.

The higher values for E_F^c against the E_F of the slab models (see Table 1) indicate that flakes have a less oxidising power than the correspondent slab surfaces. As shown in Fig. S8 of the SI, this increase, combined with the lower bandgap values, modifies the band alignment of the flakes, switching it up and narrowing it compared to the slab models.[15] In principle, this makes the MXene flakes studied here unsuitable candidates to
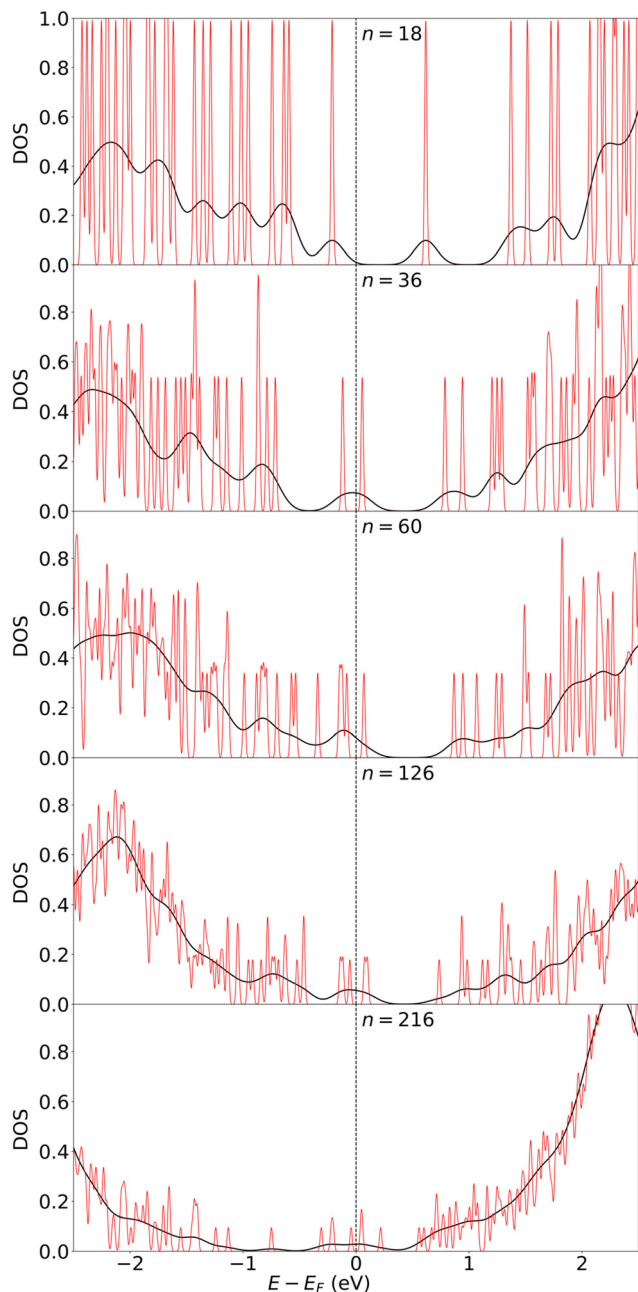
Fig. 7 Total DOS of $(Sc_2CO_2)_{18}$, $(Sc_2CO_2)_{36}$, $(Sc_2CO_2)_{60}$, $(Sc_2CO_2)_{126}$, and $(Sc_2CO_2)_{216}$ flakes represented with 0.1 and 0.01 eV Gaussian smearing in black and red lines, respectively. All densities within the displayed energy window have been normalised to 1. Fermi level, E_F, has been set to 0 on the total DOS and it is shown as a dashed black line.

Table 1 Corrected bandgap values for the largest MXene flake of each metal and their corresponding periodic model bandgap (all energy values in eV)[a]

		Flake			Slab[20]	
		n	E_g^c	E_F^c	E_g	E_F
Group III	Sc	216	2.72	−4.65	3.79	−5.59
	Y	168	2.29	−4.01	3.11	−4.74
Group IV	Ti	216	1.41	−6.32	1.64	−6.60
	Zr	216	1.57	−5.07	2.26	−6.18
	Hf	168	0.88	−4.58	2.74	−5.06
Group VI	Cr	90 (90)	0.00 (0.00)	−6.42 (−6.87)	1.27 (0.66)	−8.36 (—)
	Mo	177	0.00	−6.56	0.64	—
	W	195	0.00	−5.92	0.63	—

[a] Corrected bandgap values, E_g^c, and Fermi levels, E_F^c, obtained for the largest available $(M_2CO_2)_n$ flakes. Group III and IV MXenes present ABC stacking, while Mo and W-based MXenes show ABA stacking. For Cr, both stackings are shown, with ABA values indicated in parentheses.
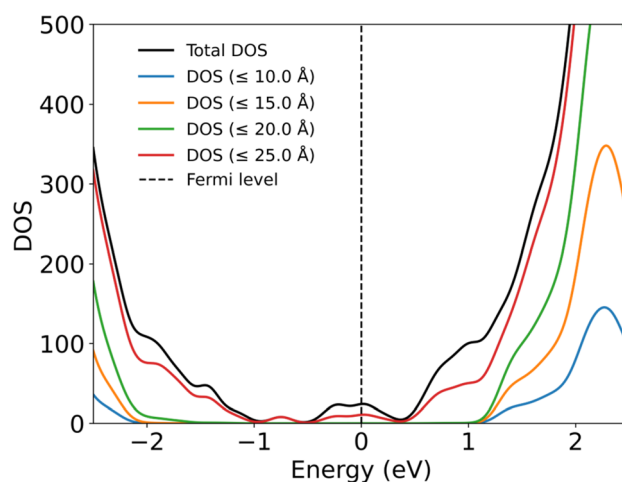
Fig. 8 Total and partials DOS of $(Sc_2CO_2)_{216}$ flake represented in black, and blue, orange, green and red, respectively. E_F has been set to 0 on the total DOS and it is shown as a dashed black line.

photocatalyse the water splitting reaction. However, the E_F^c energies lie between 0.28 and 1.94 eV above those obtained for the slab models, progressively approaching the slab values as the flakes increase in size. Since the particles studied here fall into the small size regime (diameters smaller than 10 nm), it is expected that in the limit of sufficiently large flakes, both reactions could fall within the bandgap, thereby enabling the water splitting process.

In summary, the present study introduces a more realistic explanation of the MXene flake structure *via* finite system approach, taking into account geometrical and structural distortions while observing bulk-like behaviour on central regions. This work merges the HOMO–LUMO and band structure approach for finite MXene flakes giving an explanation for the persistent metallic character of Group VI flakes, and the smaller bandgap values on Groups III and IV when comparing with periodic studies. From all studied O-terminated MXene flakes, those containing Zr are especially relevant since their bandgaps land close to or within the visible spectrum range (from 1.8 to 3.1 eV), both for the small-sized particles ($n < 90$ or 3 nm), and the larger particles that follow the asymptotic regime, with a bandgap in the centre of the particle of 1.6 eV. Large ($n > 90$) flakes of Sc and Y are also good candidates for photocatalytic applications, together with a Hf flake contain-

ing 36 stoichiometric units. This agrees with previous periodic slab model calculations, that concluded that Zr, Sc, Y, and Hf O-terminated 2D MXenes showed optimal bandgaps for photo-catalytic purposes.[20]

4. Conclusions

In this work, the structural and electronic properties of 176 MXene flakes have been investigated, including both pristine (M_2C) and O-terminated (M_2CO_2) structures, with M = Sc, Y, Ti, Zr, Hf, V, Nb, Ta, Cr, Mo, and W. For each metal, several structures were modelled following Wulff's construction rules and optimised using DFT with the PBE exchange–correlation functional. Regarding the convergence of the flakes, all metals exhibit an excellent linear tendency in the energy per unit when plotted against the inverse square root of the particle's size, which indicates the predominance of the central periodic-like structure over the lateral deformed edges when flakes become larger. Flakes containing more than 90 stoichiometric units, or above 3 nm of width, show asymptotic behaviour to the periodic MXene, indicating that their central regions replicate the structural properties of periodic systems.

Structurally, flakes have been compared with periodic systems, relating average distances between carbons, $d(CC)$, and between metal atoms; $d(M_{top}M_{top})$ and $d(M_{bot}M_{bot})$, with the structural parameter a. Overall results show similar values between flakes and periodic systems. Further analysis shows better agreement with periodic data between central atoms while deviations are seen at edge regions. An increment of thickness along periods and groups in accordance with atomic radii is observed for M_2C flakes. For M_2CO_2 flakes, thickness depends on the functionalisation site, being H_M functionalised structures the most similar to periodic structures. While most pristine flakes present planar structure, Ti, V and Cr flakes show "three-up/three-down" or global edge bending. Upon functionalisation, all ABC-stacked H_M flakes present "three-up/three-down" bending structures, while Sc and Y flakes adopt U-shaped bending, with O occupying H_M sites on the inside and H_X sites on the outside surface.

From the electronic perspective, metallic behaviour is observed for M_2C or M_2CO_2 flakes when using PBE functional, with some exceptions arising when hybrid PBE0 functional is employed. Small or no bandgaps are observed for large M_2CO_2 flakes since gap states appear due to edge defects. By isolating the contribution of the central atoms in the DOS, semiconducting behaviour has been observed on Sc, Y, Zr, and Hf metal based M_2CO_2 flakes. Nevertheless, the resulting bandgap values remain lower than those obtained from periodic systems due to subtle structural distortions in the central atoms induced by the finite size of the flakes. Using this correction, the alignment of the valence and conduction bands with respect to the water splitting half-reactions evolves favourably as flakes grow, expecting to encompass both reactions for sufficiently large flakes, thereby enabling the water splitting reaction in these systems.

Conflicts of interest

There are no conflicts to declare.

Data availability

The data supporting this article have been included as part of the supplementary information (SI). Supplementary information is available. See DOI: https://doi.org/10.1039/d6nr00506c.

Specific data files (files or atomic models) related to this study are available upon request from the corresponding author.

Acknowledgements

References

1 K. S. Novoselov, A. K. Geim, S. V. Morozov, D. Jiang, Y. Zhang, S. V. Dubonos, I. V. Grigorieva and A. Firsov, *Science*, 2004, **306**, 666–669.

2 A. K. Geim, *Science*, 2009, **324**, 1530–1534.

3 S. Roy, *et al.*, *Adv. Mater.*, 2021, **33**, 2101589.

4 S. Manzeli, D. Ovchinnikov, D. Pasquier, O. V. Yazyev and A. Kis, *Nat. Rev. Mater.*, 2017, **2**, 17033.

5 B. Anasori and M. Naguib, *MRS Bull.*, 2023, **48**, 238–244.

6 M. S. Lohse and T. Bein, *Adv. Funct. Mater.*, 2018, **28**, 1705553.

7 V. Shanmugam, R. A. Mensah, K. Babu, S. Gawusu, A. Chanda, Y. Tu, R. E. Neisiany, M. Försth, G. Sas and O. Das, *Part. Part. Syst. Charact.*, 2022, **39**, 2200031.

8 A. J. Mannix, B. Kiraly, M. C. Hersam and N. P. Guisinger, *Nat. Rev. Chem.*, 2017, **1**, 14.

9 M. Naguib, J. Halim, J. Lu, K. M. Cook, L. Hultman, Y. Gogotsi and M. W. Barsoum, *J. Am. Chem. Soc.*, 2013, **135**, 15966–15969.

10 J. Low, L. Zhang, T. Tong, B. Shen and J. Yu, *J. Catal.*, 2018, **361**, 255–266.

11 D. Dolz, R. De Armas, P. Lozano-Reis, Á. Morales-García, F. Viñes, R. Sayós and F. Illas, *ChemCatChem*, 2024, **16**, e202400122.

12 M. Naguib, M. Kurtoglu, V. Presser, J. Lu, J. Niu, M. Heon, L. Hultman, Y. Gogotsi and M. W. Barsoum, *Adv. Mater.*, 2011, **23**, 4248–4253.

13 J. C. Lei, X. Zhang and Z. Zhou, *Front. Phys.*, 2015, **10**, 276–286.

14 M. Khazaei, *et al.*, *Solid State Mater. Sci.*, 2019, **23**, 164–178.

15 D. Ontiveros, S. Vela, F. Viñes and C. Sousa, *Energy Environ. Mater.*, 2024, **7**, e12774.

16 M. Downes, C. E. Shuck, R. W. Lord, M. Anayee, M. Shekhirev, R. J. Wang, T. Hryhorchuk, M. Dahlqvist, J. Rosen and Y. Gogotsi, *ACS Nano*, 2023, **17**, 17158–17168.

17 M. Downes, C. E. Shuck, B. McBride, J. Buse and Y. Gogotsi, *Nat. Protoc.*, 2024, **19**, 1807–1834.

18 M. Naguib, O. Mashtalir, J. Carle, V. Presser, J. Lu, L. Hultman, Y. Gogotsi and M. W. Barsoum, *ACS Nano*, 2012, **6**, 1322–1331.

19 V. Kamysbayev, A. S. Filatov, H. Hu, X. Rui, F. Lagunas, D. Wang, R. F. Klie and D. Talapin, *Science*, 2020, **369**, 979–983.

20 D. Ontiveros, F. Viñes and C. Sousa, *J. Mater. Chem. A*, 2023, **11**, 13754–13764.

21 B. Anasori and Y. Gogotsi, *Graphene 2D Mater.*, 2022, **7**, 75–79.

22 N. García-Romeral, Á. Morales-García, F. Viñes, I. de P. R. Moreira and F. Illas, *Phys. Chem. Chem. Phys.*, 2023, **25**, 31153.

23 N. García-Romeral, Á. Morales-García, F. Viñes and F. Illas, *Nanoscale*, 2025, **17**, 22849–22859.

24 S. Zhao, W. Kang and J. Xue, *J. Mater. Chem. C*, 2015, **3**, 879–885.

25 L. Hong, R. F. Klie and S. Öğüt, *Phys. Rev. B*, 2016, **93**, 115412.

26 Y. Morency and A. Vojvodic, *Nanoscale*, 2025, **33**, 19210–19219.

27 A. Lipatov, M. Alhabeb, M. R. Lukatskaya, A. Boson, Y. Gogotsi and A. Sinitskii, *Adv. Electron. Mater.*, 2016, **2**, 1600255.

28 J. Sui, X. Chen, Y. Li, W. Peng, F. Zhang and X. Fan, *RSC Adv.*, 2021, **11**, 16065–16082.

29 H. Shi, P. Zhang, Z. Liu, S. W. Park, M. R. Lohe, Y. Wu, A. S. Nia, S. Yang and X. Feng, *Angew. Chem., Int. Ed.*, 2021, **60**, 8689–8693.

30 Q. Xue, H. Zhang, M. Zhu, Z. Pei, H. Li, Z. Wang, Y. Huang, Y. Huang, Q. Deng, J. Zhou, S. Du, Q. Huang and C. Zhi, *Adv. Mater.*, 2017, **29**, 1604847.

31 G. Xu, Y. Niu, X. Yang, Z. Jin, Y. Wang, Y. Xu and H. Niu, *Adv. Opt. Mater.*, 2018, **6**, 1800951.

32 B. Vénosová and F. Karlický, *Nanoscale Adv.*, 2023, **5**, 7067–7076.

33 G. Wulff, *Z. Kristallogr.*, 1901, **34**, 449–531.

34 J. M. Rahm and P. Erhart, *J. Open Source Softw.*, 2020, **5**, 1944.

35 V. Blum, R. Gehrke, F. Hanke, P. Havu, V. Havu, X. Ren, K. Reuter and M. Scheffler, *Comput. Phys. Commun.*, 2009, **180**, 2175–2196.

36 V. Havu, V. Blum, P. Havu and M. Scheffler, *J. Comput. Phys.*, 2009, **228**, 8367–8379.

37 J. P. Perdew, M. Ernzerhof and K. Burke, *J. Chem. Phys.*, 1996, **105**, 9982.

38 R. L. Johnston, *Atomic and Molecular Clusters*, Taylor and Francis, London, 2002.

39 F. Viñes, O. Lamiel-García, F. Illas and S. T. Bromley, *Nanoscale*, 2017, **9**, 10067–10074.

40 J. P. Perdew, K. Burke and M. Ernzerhof, *Phys. Rev. Lett.*, 1996, **77**, 3865–3868.